Article

Not peer-reviewed version

3D Printing of Optimized Titanium Scaffold for Bone Replacement

Parvathi Nathan *, Siaw Meng Chou, Wai Yee Yeong

Posted Date: 22 April 2025

doi: 10.20944/preprints202504.1850.v1

Keywords: 3D printing; Ti64; bone replacement; pore size; lattice; SLM

 doi:10.20944/preprints202504.1850.v1

Article

3D Printing of Optimized Titanium Scaffold for Bone Replacement

Parvathi Nathan [1,*], Siaw Meng Chou [1,2] and Wai Yee Yeong [1,2]

[1] Singapore Centre for 3D Printing, School of Mechanical & Aerospace Engineering, Nanyang Technological University, Singapore 639798; msmchou@ntu.edu.sg (S.M.C); wyyeong@ntu.edu.sg (W.Y.Y)

[2] School of Mechanical & Aerospace Engineering, Nanyang Technological University, Singapore 639798

* Correspondence: parvathi002@e.ntu.edu.sg or parvathi.nathan9@gmail.com

Abstract: Critical-sized bone defects or CSDs results from bone loss due to trauma, tumour removal, congenital defects or degenerative diseases. Though autologous bone transplantation is the current gold standard in treating CSDs, its limitations include donor-site morbidity, unavailability of donor bone tissues, risk of infection, and mismatch between the bone geometry and the defect site. Customized scaffolds fabricated using 3D printing and biocompatible materials can provide mechanical integrity and facilitates osseointegration. Ti-6Al-4V aka Ti64 is one of the most widely used commercial alloys in orthopedics. To avoid elastic modulus mismatch between bones and Ti64, it is imperative to use porous lattice structures. Porous lattices using diamond, cubic and TPMS (triply periodic minimal surface) gyroid unit cells were designed for 300, 600 and 900 μm pore sizes and 3D printed using selective laser melting (SLM). Compression and in-vitro tests were conducted to study the impact of pore size and unit cell variation on mechanical and biological behaviour. Results showed that the compressive properties decreased with increase in pore sizes. The biological evaluation reported maximum cell adherence in lower pore sizes with gyroid samples exhibiting statistically significant ($p < 0.01$) increase in cell proliferation.

Keywords: 3D printing; Ti64; bone replacement; pore size; lattice; SLM

1. Introduction

Additive Manufacturing (AM) aka 3D printing (3DP) technology is a revolutionary and efficacious alternative to conventional manufacturing techniques. 3DP covers a wide range of applications such as aerospace, biomedical, electronics and digital control, food, biotechnology etc. The core advantages of 3DP includes minimization of material wastage, freeform fabrication, fabrication of complex shapes such as lattices and enhanced productivity due to reduction in various production steps [1,2]. 3DP has been currently used in the manufacture of medical devices, especially bone scaffolds, implants and assistive/rehabilitation devices. The process of 3DP customized bone scaffolds has been illustrated in Figure 1. Although human bones could regenerate and self-repair, this is limited and dependent on the extent of the injury, site of bone defect, age, gender, and other factors [3–7]. Bone damage exceeding its acceptable limit may lead to loss of self- regeneration, thereby calling for artificial repair by means of bone replacement [8–11]. Bone scaffolds are capable of functional and structural repair and regeneration of bone defects. There have been extensive research advancements in the field of orthopaedic scaffolds, however, repair/treatment of bone defects is one of the key challenges in the realm of orthopaedics and regenerative medicine [11]. Bone defects could be caused due to tumour, trauma or malunion during fracture healing should be treated using surgical intervention and therapeutic treatment; surgical intervention involves the use of permanent or temporary bone scaffolds [11,12]. Tissue lesions resulting from accidents, trauma, tumours, infection, congenital defects, ageing etc. will need artificial scaffolds or transplantation for recovery. The potential of customized scaffold manufacture using 3DP has opened new horizons in the biomimetic metallic scaffold realm and reconstruction of complex bony defects [13].

 doi:10.20944/preprints202504.1850.v1

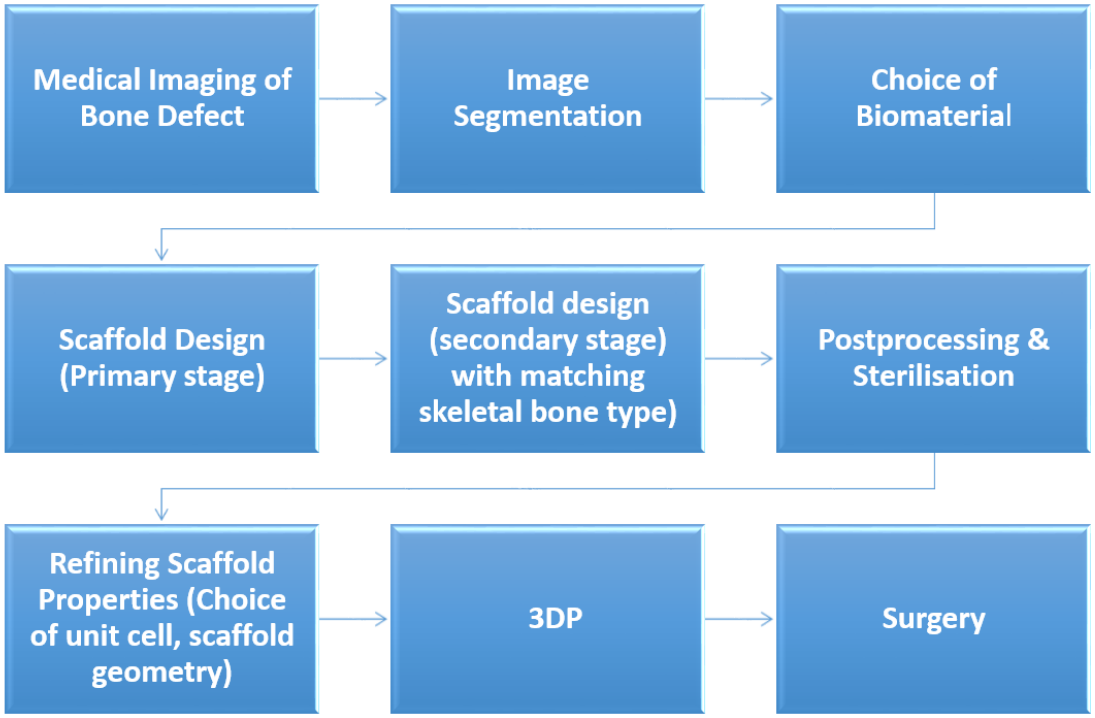

Figure 1. Flowchart of 3DP Customized Bone Scaffold.

Critical-sized bone defects (CSD) (typically > 5 cm in diameter) or those defects that do not heal spontaneously during the lifetime of the patient require support in the form of biomaterial scaffolds [5,14–17]. Despite adequate stabilization, bone loss greater than twice the diameter of the long bone diaphysis may potentially result in non-union [15]. The current gold standard in the treatment of bone defects is autografts or autologous bone transplantation which contain a scaffold with osteogenic properties [15–18]. The limitations of autologous transplantation or autografts include limited harvesting, donor-site morbidity, unavailability of donor bone tissues, risk of infection, and mismatch between the bone geometry and the defect site [16–18]. Porous metallic scaffolds mimic the structure of natural bone in addition to providing ample mechanical integrity- this makes it suitable for treatment of CSDs [19]. One of the most widely used commercial alloys in bone tissue engineering (BTE) is Ti6Al4V aka Ti64. Ti64 has demonstrated its biocompatibility and bio-inert nature, making it apposite for long-term application [20–23]. Ti64 has been widely used in dentistry and orthopaedic applications such as dentures, hip, knee and other hard tissue scaffolds, maxillofacial and oral repair, cranioplasty, plates, screws etc. [24,25].

Ti64 was used in the current study due to its industrial, clinical, and regulatory acceptance. The current study incorporated lattices into the 3DP scaffold to optimize its performance by reducing stress shielding/elastic modulus mismatch and facilitating osseointegration. The Young's modulus of an ideal bone replacement should be as close to that of the human bone as possible for effective load distribution. The type of lattice structure, pore size, porosity, pore interconnectivity was designed and evaluated for mechanical and biological optimization for bone replacement. The objective is to create a scaffold/bone block with adequate osseointegration ability, mechanical strength, and porous structure to facilitate bone ingrowth.

2. Materials and Methods

2.1. Feedstock Powder

The samples used for the current study were fabricated using gas atomised Ti-6Al-4V extra low interstitial (ELI) powder supplied by SLM Solutions, Germany. The chemical composition of the

 doi:10.20944/preprints202504.1850.v1

powders as provided by the supplier is detailed in Table 1. The powder morphology was observed to be predominantly spherical (Figure 2).

Table 1. Chemical composition of SLM Grade 23 Ti64 ELI.

Element	Composition (%)
Al	6.46
V	4.24
Fe	0.17
N	0.01
C	0.007
H	0.002
Ti	≈ 90

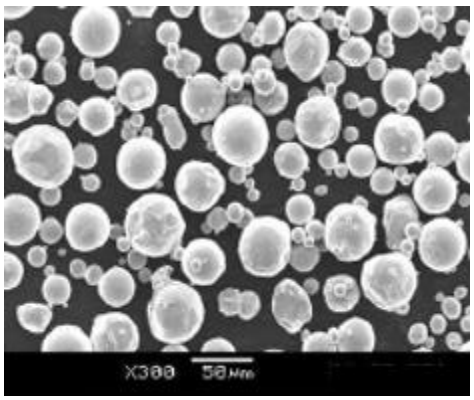

Figure 2. Morphology of Ti64 particles (SEM).

2.2. Sample Design and Fabrication

Cylindrical (⌀10 mm x h 20 mm) and disc (⌀10 mm x h 4 mm) samples were designed for the mechanical and biological tests respectively. The cylindrical samples were designed as per the ASTM E9 standard (Compression Testing of Metallic Materials at Room Temperature) which also satisfies the ISO 13314: 2011 standard for compression testing of porous metal samples. The porous scaffolds were designed using nTopology version 3.29.3. Three different unit cells (diamond, cube and TPMS gyroid) with three different pore sizes (300, 600, 900 µm) were designed (Figure 3).

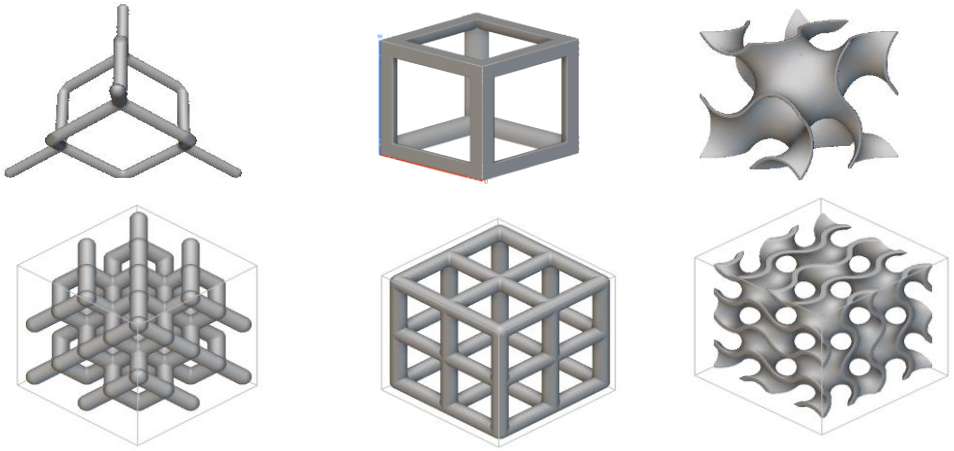

Figure 3. Unit Cells used in this study and the 2x2x2 lattices: (**a**) Diamond, (**b**) Cubic, (**c**) Gyroid.

 doi:10.20944/preprints202504.1850.v1

Diamond and cube lattices are strut-based lattices and TPMS gyroid is a sheet-based lattice. The samples aka scaffolds were fabricated using SLM 280 (Nikon SLM Solutions, Germany) located at Nikon SLM Solutions Pte Ltd, Singapore. The laser source is YLR-100-SM single-mode CW ytterbium fiber laser (1064 – 1100 nm). Following the fabrication, the Ti64 samples were subjected to wire-cutting and washed with distilled water. This was followed by sterilization using ethanol.

2.3. Sample Characterization

The morphological characterisation of the 3DP Ti64 scaffolds was conducted using dry-weighing, SEM imaging and micro-CT scanning. The surface morphology was characterised using the JEOL (JSM-5600LV). The pore and strut size were analysed using SEM and μ - CT. The porosity (by measuring relative density) was also measured using μ - CT and dry weighing.

2.3.1. Dry Weighing, MicroCT (μCT) Scanning and SEM

Dry weighing was conducted using the Mettler Toledo XS204. The mass of the samples (n = 5) was thrice at room temperature and normal atmospheric conditions. The bulk density of Ti64 is 4430 kg/m3. The results obtained from the dry weighing was used for calculating the porosity. The pore size, strut size and porosity were measured using the Skyscan 1173 MicroCT equipment with a voltage of 130 kV and current of 60 μA. The morphological characterisation is reported in Tables 2–4.

Table 2. Sample Characterisation of Diamond Samples.

	P300	**P600**	**P900**
Designed Top View (CAD)	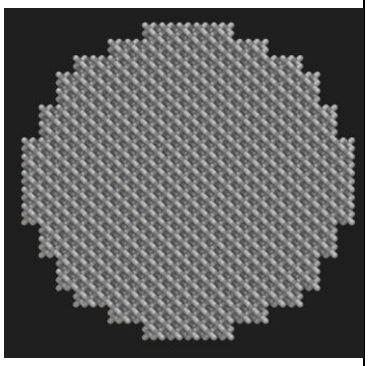	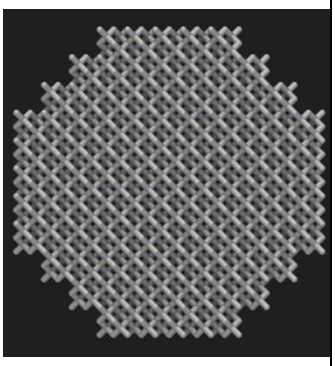	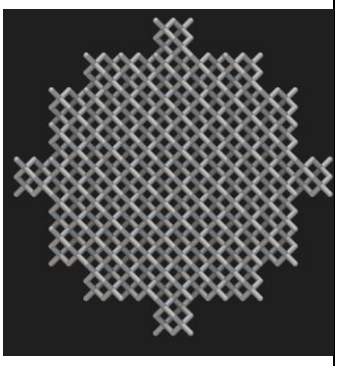
SEM Images	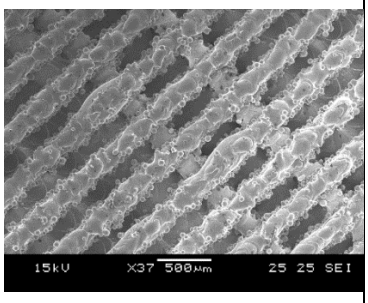	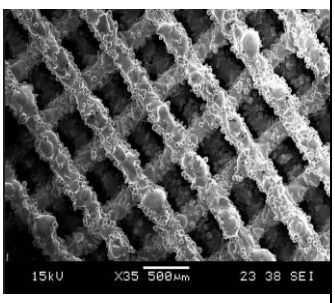	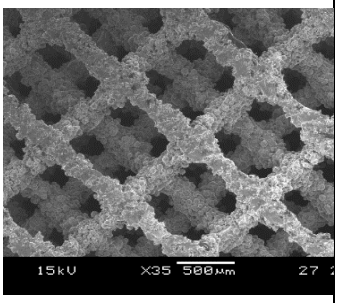
Designed Strut Size (μm)	200	200	200
Measured Strut	165 ± 3.7	185 ± 6.6	140 ± 7.5

 doi:10.20944/preprints202504.1850.v1

Size (SEM) (μm) (n = 5)			
Measured Strut Size (μCT) (n = 2)	158 ± 11	172 ± 9.5	150 ± 6
Measured Pore Size (SEM) (μm) (n = 5)	258 ± 5.9	563 ± 7.5	846 ± 10
Measured Pore Size (μCT) (μm) (n = 2)	230 ± 1.9	524 ± 4.8	810 ± 2.6
Porosity (CAD) (%)	53.34	80.88	90.13
Measured Porosity (%) (μCT)	45.78	72.65	81.34

 doi:10.20944/preprints202504.1850.v1

Table 3. Sample Characterisation of Cubic Samples.

	P300	P600	P900
Designed Top View (CAD)	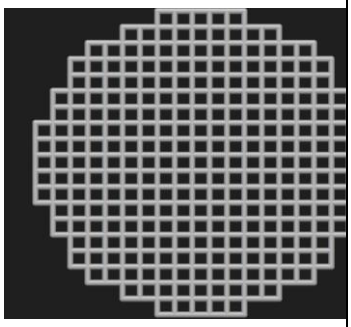	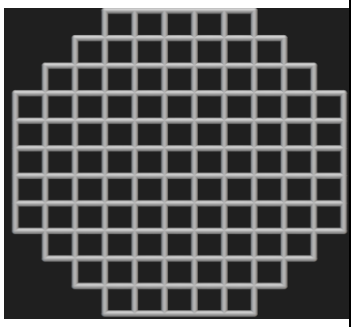	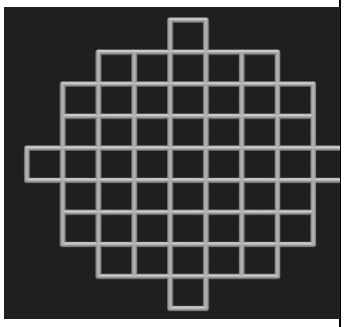
SEM Images	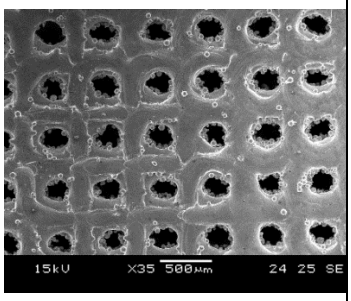	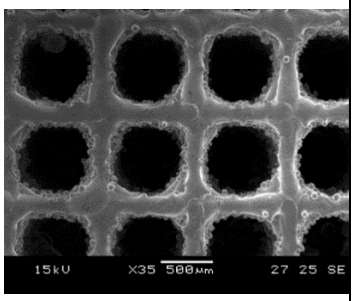	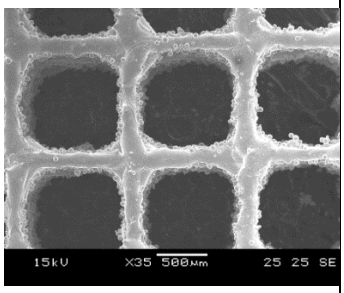
Designed Strut Size (µm)	200	200	200
Measured Strut Size (SEM) (µm) (n = 5)	181 ± 9.7	191 ± 5.4	186 ± 5.3
Measured Strut Size (µ-CT) (n = 2)	164 ± 5.5	177 ± 2.9	180 ± 4.6
Measured Pore Size (SEM) (µm) (n = 5)	268 ± 6.9	533 ± 2.7	855 ± 3.6
Measured Pore Size (µCT)	228 ± 6.2	557 ±11.6	830 ± 6.8

 doi:10.20944/preprints202504.1850.v1

(µm) (n = 2)			
Porosity (CAD) (%)	75.17	89.94	94.38
Measured Porosity (%) (µCT)	62.45	85.78	90.54

Table 4. Sample Characterisation of Gyroid Sample.

	P300	**P600**	**P900**
Designed Top View (CAD)	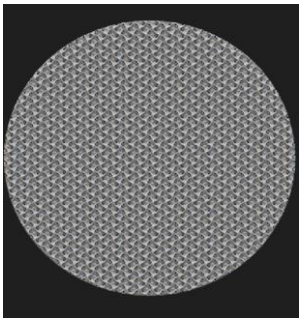	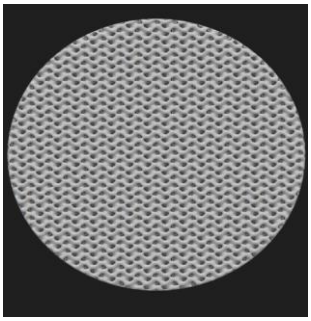	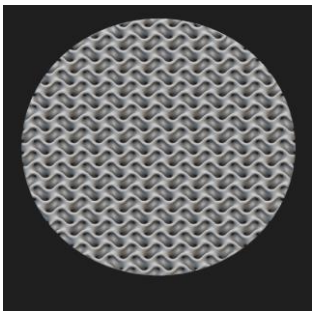
SEM Images	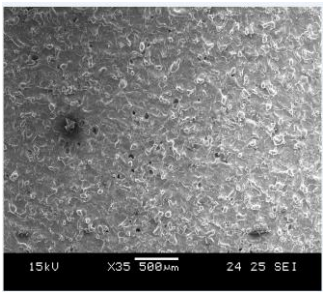	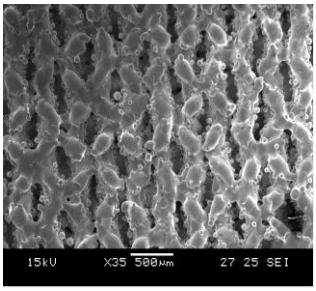	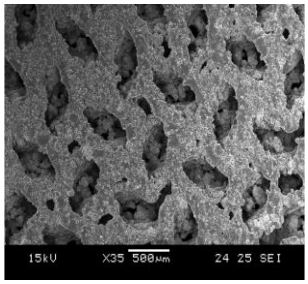
Measured Pore Size (µCT) (µm) (n = 2)	NA*	358 ± 12.5	630 ± 6.8
Theoretical Porosity (CAD) (%)	34.06	67.66	78.45
Measured Porosity (%) (µ CT)	24.54	45.67	67.87

* Could not be measured due to fully fused powder (nil pore visibility).

2.3.2. Mechanical Testing

The specimens were tested in compression until failure to determine the mechanical properties. Compression tests were carried out using the Shimadzu Autograph AG-X Plus mechanical testing

 doi:10.20944/preprints202504.1850.v1

machine with a maximum loading cell of 100kN.The ISO 13314:2011 (Ductility testing — Compression test for porous and cellular metals) was used. The ultimate compressive strength (UCS/ σ_{max}), yield strength (σ_y) and Young's modulus (E) were obtained from the stress strain curves. As per ISO 13314: 2011, UCS is the first maximum compressive strength. The concept closest to Young's modulus is the elastic gradient, which is the gradient of the elastic straight line between σ_{70} and σ_{20}. It was noted that the plateau stress is equivalent to the yield stress, which was determined using the arithmetical mean of the stresses between 20% and 40% of the compressive strain.

2.3.3. In Vitro Biological Evaluation

HOBs (human osteoblasts, 500,000, cryopreserved) were purchased from PromoCell (C-12720, Germany). These cells are fully differentiated osteoblasts from femoral trabecular bone tissue of a healthy donor (37 years, Caucasian female).Cells were cultured using Osteoblast culture medium (PromoCell, Germany) supplemented with 10% supplement mix (PromoCell, Germany) and antibiotics (1% PenStrep, Gibco, USA). The cells were cultured under standard conditions (5% CO2, 37°C). Cell medium was refreshed every 3 days without disturbing the cell monolayer. Cell passage was carried out when cell confluency reached 80%. At each passage, cells were washed with phosphate buffered saline (PBS, Gibco), detached with Trypsin EDTA (Gibco, USA) and plated in T25 cell culture flasks (Thermo Fisher Scientific, USA) at a density of 15,000 cells/cm^2. Final cell densities of 2.5 × 105 (low) and 1 × 106 cells/ml (high). Osteoblasts were seeded onto scaffolds using drop method in a 24 –well plate using 0.1 ml of cell solution. To permit cell attachment, the scaffolds were placed in an incubator for 2 hours. This was followed by adding 2ml of supplemented growth media.

Cell adherence using fluorescence microscopy was performed to understand the extent of osteoblast adherence on 3DP Ti64 scaffolds using 4', 6-Diamidino-2-Phenylindole, Dihydrochloride (DAPI, 0.01 mg/ml in PBS) (Invitrogen, United States). Live cells were fixed using 4% paraformaldehyde (PFA); 2 ml of 4% PFA was added to the scaffolds at room temperature. The cell nuclei (stained in blue) would be observed. Leachate analysis in the current study involved Ti64 scaffolds immersion in the cell culture medium followed by seeding of HOBs to check for cytotoxicity. The cytotoxicity of the cells exposed to Ti64 for 14 days was assessed using DAPI+ fluorescence microscopy.

Cell proliferation was conducted using the MTT (3-(4,5-dimethylthiazol-2-yl)-2,5-diphenyl-2H-tetrazolium bromide) Cell Proliferation and Cytotoxicity Assay Kit (MyBioSource, USA). The assay was conducted as per the manufacturer's instructions. The optical density (OD) value was measured with a microplate reader at 570 nm. The colour intensity is directly proportional to the number of viable cells and the rate of cell proliferation, with darker colour indicating greater cell proliferation and lighter colour indicating cytotoxicity [26].

2.4. Statistical Analysis

The data from the mechanical and biological tests were analysed using Microsoft excel and SPSS Statistics 29.

3. Results and Discussion

3.1. Sample Characterization

Figure 4 has depicted the CAD and measured porosity of the 3DP scaffolds.

 doi:10.20944/preprints202504.1850.v1

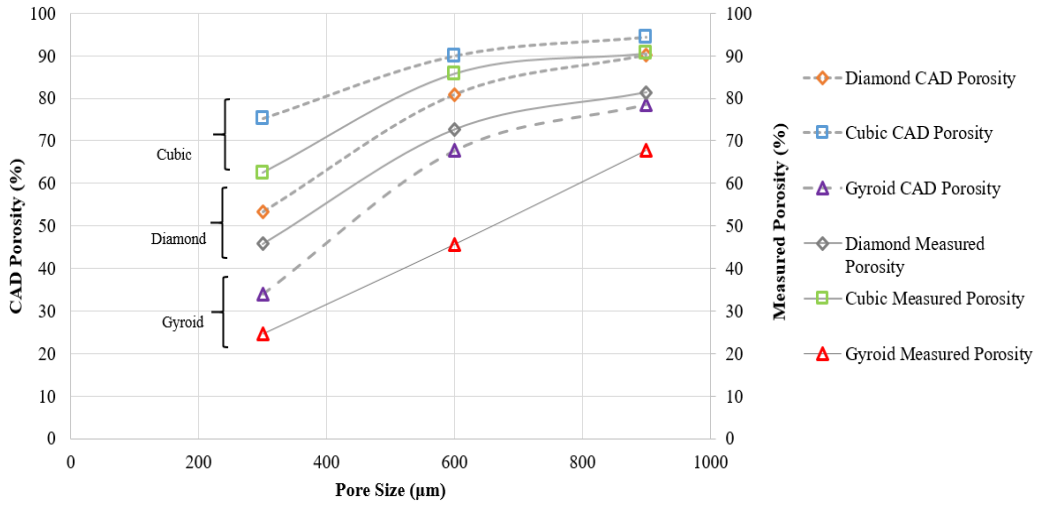

Figure 4. CAD Porosity and Measured Porosity of Samples.

The difference in the porosity of the designed and as-built samples could be due to fusion of the powders and subsequent adhesion. The porosity of the as-built samples is lower than the designed samples in all the samples. The pore size of the CAD and as-built samples is depicted in Figure 4. The deviation of the measured porosity from the CAD porosity is predominant for the TPMS gyroid samples compared to the strut-based diamond and cubic samples. For the strut-based lattices, lower porosity samples deviated more from the CAD porosity.

3.2. Compressive Properties

Table 5 has the relevant data from the sample compression tests.

Table 5. Mechanical Characterisation of the 3DP Ti64 samples from Compression tests (n = 5).

Scaffold Type	Pore Size (µm) (Porosity (%))	Peak Force (kN)	Ultimate Compressive Strength (MPa)	Young's Modulus (GPa)	Yield Stress (MPa)
Diamond	300 (45.78)	57.33 ± 2.56	729.98 ± 32.61	10.72 ± 0.40	450.96 ± 31.17
	600 (72.65)	5.33 ± 0.17	68.27 ± 2.56	2.76 ± 0.14	45.43 ± 3.38
	900 (81.34)	2.22 ± 0.04	27.41 ± 0.55	1.01 ± 0.03	17.5 ± 0.56
Cube	300 (62.45)	21.21 ± 0.5	270.10 ± 6.33	10.03 ± 1.43	260.41 ± 22.44
	600 (85.78)	5.97 ± 0.3	89.33 ± 4.97	4.88 ± 0.32	51.87 ± 5.41
	900 (90.54)	3.12 ± 0.11	38.25 ± 1.39	2.26 ± 0.41	14.86 ± 1.24
Gyroid	300 (24.35)	**NA			
	600 (45.67)	73.78 ± 5.64	925.4 ± 72.00	13.18 ± 0.85	478.16 ± 8.29
	900 (67.87)	22.55 ± 0.41	282.78 ± 6.05	7.83 ± 0.76	238.18 ± 10.96

**Specimens not porous, hence considered unsuitable for bone replacement.

During compression testing of D300 samples, shear occurred in all 5 samples. The D300 (porosity < 50%) and D600 (porosity > 50%) suitable for cortical bone applications. Unlike the former, the latter is not suitable for high load-bearing applications such as in the diaphysis region or distal region of the femur. The D900 (with porosity > 50%) sample is closer to the range of the trabecular bone's modulus and can be considered for non-load bearing scaffolds. This asserts the importance of pore size in reducing the elastic modulus mismatch and stress-shielding for bone scaffolds. Similar trends were also noted for the UCS and σ_y. A bone scaffold biomaterial should have high yield strength and

 doi:10.20944/preprints202504.1850.v1

fatigue strength to prevent failure under cyclic loading; hence apposite yield strength is necessary. As per the findings of Taniguchi et al. (2015) [27], pore size had significant impact on the biological and compressive properties of 3DP commercially pure Ti diamond lattices. Similar to the current study, the samples of 300, 600 and 900 μm pore size was subjected to mechanical testing and E in the range of cancellous bone was reported. Contradictory to the results of the current study, an increase in pore size reported minor increase in the modulus and yield strength of the scaffold; this could be because the scaffolds were designed for a fixed porosity and an increase in pore size could have been compensated by increase in strut size. The results reported by Huang et al. (2022) [28] was similar to our current study. Table 6 has compared the findings of our study and similar studies [27,29–34]. It has to be noted that as the strut size in our study was constant, an increase in pore size would mean an increase of porosity.

Table 6. Comparison of the findings the current study & similar studies (diamond unit cell).

Author (year)	Technology, Material & Unit Cell	Scaffold Architecture	Comments
Current Study (2025)	SLM, Ti64, Diamond, Cubic, TPMS Gyroid	Pore size : 300, 600, 900 μm (fixed strut size)	$E_{D300} > E_{D600} > E_{D900}$ Similar trend for σ_y and UCS
Taniguchi et al. (2016) [27]	SLM, cp- Ti, Diamond	Pore size : 300, 600, 900 μm (constant porosity 65%)	$E_{900} > E_{600} > E_{300}$
Pei et al. (2017) [29]	SLM, Ti64, Diamond	Strut diameter : 200, 250,300,350, 400 μm with constant pore size (~ 630 μm)	Increase in strut diameter increased E, UCS ◎ linear trend
Zhang et al. (2018) [30]	SLM, Ti64, Diamond	Strut diameter : 200, 250,300,350, 400 μm strut diameter with constant pore size (~ 650 μm)	Increase in strut diameter increased E, UCS ◎ linear trend
Yavari et al. (2014) [31]	SLM, Ti64, Diamond, Cubic, Truncated cuboctahedron	Pore size : 600 – 1452 μm 63 – 90% porosity	Increase in strut thickness increased E, UCS ◎ linear trend
Liu et al. (2018) [32]	SLM, Ti64, Diamond	Relative density of 1.28 to 18.6% Varying strut size ,optimised radius	Increase in strut diameter, optimised radius increased E
Wally et al. (2019) [33]	SLM, Ti64, Diamond, functionally graded structures (FGS), hexagonal prism	Non-graded pore size : 400 – 650 μm Strut diameter : 300 - 400 μm Varying pore and strut size for FGS	Overall linear relationship in the elastic region and then plastic yield plateau Graded and non-graded structures exhibited similar E, σ_y

 doi:10.20944/preprints202504.1850.v1

			Increase in strut diameter increased E, UCS Increase in porosity, pore size ⊚ increased E, UCS
Deng et al.(2021) [34]	SLM, Ti64, Diamond, Cubic, Truncated cuboctahedron, open circular pores	Pore size : 650 µm 65 % porosity	$E_{TC} > E_C > E_D > E_{CIR}$ Similar trend for σ_y

Similar to the diamond samples, the lower pore sizes exhibited maximum modulus, yield strength and UCS in cubic samples. The C300 sample experienced failure by means of bending with potentially vertical strut failure being the reason for deformation. The C600 and C900 samples failed due to crushing. When a strut fails, the neighbouring struts in the same plane are also subjected to failure, which is a cascading phenomenon. The E for samples decreases with increasing pore size and porosity. It has to be noted that similar to the diamond samples, the cubic samples also experienced sharp decline in E on increasing the pore size from 300 to 600 µm. However, the C300 and 600 samples (> 50% porosity) had a modulus within the cortical bone range making it suitable for load-bearing applications. The C900 sample modulus is very slightly above the trabecular range, however, can be used in regions where there the proportion of trabecular bone is higher than cortical bone. Similar to the diamond samples, the C300 samples exhibited a yield stress greater than cortical bone whereas the 600 (cortical) and 900 (trabecular) µm samples were within the bone range. Results similar to the current study was reported by Choy et al. (2017) [35]. Choy et al. (2017) [35] reported that 3DP cubic samples of different strut sizes failed in a layer by layer manner. The method of collapse was same irrespective of the strut sizes. A number of research studies [36–54] have demonstrated how the change in pore size and porosity affects the mechanical properties. Benedetti et al. (2019) [54] also reported similar results. All the aforementioned research studies have detailed how increase in porosity and pore compromises the mechanical integrity. Table 7 lists the summary data of current study and other related studies [31,34,54–56] using cubic unit cell samples.

Table 7. Summary data of current study vs other similar studies (cubic unit cell).

Author (year)	Technology, Material & Unit Cell	CAD Scaffold Architecture	Comments
Current Study (2022)	SLM, Ti64, Diamond, Cubic, TPMS Gyroid	Pore size : 300, 600, 900 µm (fixed strut size)	$E_{C300} > E_{C600} > E_{C900}$ Similar trend for σ_y and UCS
Ahmadi et al. (2015) [55]	SLM, Ti64, cubic (C), diamond (D), truncated cube (TC), truncated cuboctahedron (TCO), rhombic dodecahedron (RD), and rhombi cuboctahedron (RCO)	Pore size : 600 – 1452 µm Strut size : 277 – 720 µm	Compressive properties increased with increase in structure relative density Rhombic cuboctahedron and rhombic dodecahedron ⊚⊚highest and lowest compressive properties at relative density < 0.2 Cubic samples relatively stable

 doi:10.20944/preprints202504.1850.v1

Yavari et al. (2015) [31]	SLM, Ti64, Diamond, Cubic, Truncated cuboctahedron	Pore size : 600 – 1452 µm Strut size : 277 – 720 µm	Fatigue life decreased as the porosity of the structure increased Cubic unit cell samples did not fail at endurance limit ◎ maximum fatigue strength mechanical properties of the truncated cuboctahedron◎ similar for similar porosities
Benedetti et al. (2019) [54]	SLM, Ti64, cubic (C), star (S) and cross (X) structures	Pore size: 700 – 1500 µm Strut size – 200 - 500 µm	Maximum stiffness reported by cubic samples Collapse of vertical struts Sharp decrease of stress during plastic deformation
Deng et al. (2021) [34]	SLM, Ti64, cubic (C), diamond (D), truncated cube (TC), circular pores	Pore size : 650 µm Porosity : 65%	$E_{TC} > E_{CU} > E_{DIA} > E_{CIR}$
Wang et al.(2022) [56]	SLM, Ti64 cubic, octet, and TPMS gyroid	Pore size : 200 – 500 µm Porosity – 40%, 50%, 60%	Mechanical stability: TPMS > octet > cubic

As far as the TPMS gyroid samples are concerned, only data pertaining to G600 and G900 were considered; G300 samples were not porous and hence its mechanical data has not been discussed. The gyroid samples in the current study are not suitable for trabecular bone applications. Similar to D300, G600 sample fractured by means of shear. The G900 sample also experienced failure due to shear; in addition, it is the only sample that exhibited failure before 20% compressive strain. The study by Bobbert et al. (2017) [57] on the compressive performance of 4 types of TPMS structures (primitive (P), I-WP (I), gyroid (G), and diamond (D) found that an increase in the pore size resulted in reduction of E. Similar deformation behaviours were reported previously by Weiβmann et al., (2016) [58], Van Hooreweder et al. (2017) [59], and Zhang et al. (2018) [30]. Similar to the current study, a failure in the oblique direction was observed by Sun et al. (2022) [60]. Sun et al. (2022) [60] further reported quasi-cleavage to be the cause of fracture of the gyroid samples. Similar to our current study and other studies reviewed, a decrease in pore size was associated with greater mechanical integrity with respect to E, yield and UCS.

A similar research study by Yanez et al. (2018) [61] recommended gyroid Ti64 as a scaffold in bone defect construction. Wang et al. (2022) [56] evaluated the biomechanical properties of cubic, octet and TPMS gyroid Ti64 structures. Wang et al. (2022) found that cubic lattices were less stable compared to octet and TPMS gyroid. Similar to our study, the TPMS gyroid structures reported higher mechanical integrity for similar porosities. Unlike the porosity range of 38 – 59% used by Wang et al. (2022) [56], our G600 and G900 samples in the current study had a porosity of < 50%.

Wang et al. (2022) [56] has reported TPMS gyroid samples to have exhibited maximum stability due to the homogenous distribution of stress within the structure. Similar to our study, the TPMS gyroid samples were least affected by the variation in porosity. As expected, our TPMS gyroid samples had higher mechanical performance despite larger pore sizes. Wang et al. (2022) [56] has also reported that gyroid structures had higher E (1.85 times) compared to the cubic samples at similar

 doi:10.20944/preprints202504.1850.v1

porosity (~ 50%). With a higher porosity, the E of TPMS was 4.5 times higher. A similar study conducted by Naghavi et al. (2022) [62] compared the mechanical characteristics of TPMS diamond and gyroid Ti64 structures for bone implants. Similar to our samples design, the pore size was varied with fixed sheet thickness. However, the intra-group variation of pore sizes not uniform. Similar to our study, the increase in pore size reduced the E and σ_y of the gyroid structures. The trend was similar for TPMS diamond samples as well. Naghavi et al. (2022) reported that the stiffness of the gyroid structures varied from 4.4 – 9.54 GPa and σ_y had a range of 106 – 170 MPa. As far as the diamond samples are concerned, the scaffolds were stiffer at similar pore sizes and porosities. Barber et al. (2021) [63] aimed at comparing the TPMS gyroid and diamond with a constant porosity of 75%. They demonstrated that gyroid had a stiffness of 2.3 GPa and σ_y of 94 MPa. The TPMS diamond samples had a stiffness and σ_y of 3.1 GPa and 129 MPa, respectively.

Bobbert et al. (2017) [57] reported similar results for compression testing of TPMS structures. The compressive performance of 4 types of TPMS structures (primitive (P), I-WP (I), gyroid (G), and diamond (D) with different porosities and pore sizes and reported similar trends in mechanical properties. Sun et al. (2022) [60] compared the compression and energy absorption properties of SLM Ti64 TPMS structures and reported elastic – brittle failure mechanism. Yanez et al. (2018) [61] studied gyroid scaffolds in the range of 75 – 90% porosity in the trabecular bone range with spherical structures (normal) and ellipsoidal structures (deformed) respectively. It was reported that deformed gyroid structures reported higher compressive properties compared to normal gyroid structures of similar porosity. A similar study by Zaharin et al. (2018) [52] compared the cube and gyroid lattices of varying strut sizes/sheet thickness reported a linear decrease in the compressive modulus with an increase in the porosity and pore size. A strut diameter of 0.3 mm was recommended for bone scaffold applications. The study conducted by Li et al. (2019) [64] investigated the early osseointegration in porous Ti64 samples with TPMS unit cell and reported satisfactory results. On compressive testing, the samples reported a satisfactory compressive modulus and porosity well within the range of the cortical bone. Table 8 list summary data of current study and other related studies [52,56,57,60–62] using gyroid unit cell samples. Current results shows similar trend in the mechanical properties.

Table 8. Summary of data of current study vs other similar studies.

Author (year)	Technology, Material & Unit Cell	CAD Scaffold Architecture	Comments
Current Study (2022)	SLM, Ti64, Diamond, Cubic, TPMS Gyroid	Pore size : 300, 600, 900 μm (fixed strut size)	$E_{C300} > E_{C600} > E_{C900}$ Similar trend for σ_y and UCS Gyroid exhibited max E and UCS despite lesser porosity
Bobbert et al. (2017) [57]	SLM, Ti64, TPMS	Porosity range : 43 – 77% Pore size : 361 – 896 μm	Increase in pore size, porosity reduced E Ductile failure in gyroid
Yanez et al. (2018) [61]	SLM, Ti64, TPMS	Porosity: 75 – 90% Circular and ellipsoidal pores	Deformed gyroids had better mechanical characteristics

 doi:10.20944/preprints202504.1850.v1

Zaharin et al. (2018) [52]	SLM, Ti64, TPMS, cubic	Pore size : 300 μm, 400 μm, 500 μm and 600 μm Fixed strut size	Increase in the pore size reduced E E at 300 μm pore size close to cortical bone range for TPMS and cubic samples
Naghavi et al. (2022) [62]	SLM , Ti64, TPMS diamond and gyroid	TPMS Gyroid pore size: 600 – 1200 μm Porosity range: 54 – 72%. TPMS diamond pore size : 900 – 1500 μm Porosity range : 56 – 70%	Stiffness of the gyroid structures varied from 4.4 – 9.54 GPa σ_y - 106 – 170 MPa. TPMS diamond samples ◎ stiffer at similar pore sizes and porosities
Wang et al.(2022) [56]	SLM, Ti64 cubic, octet, and TPMS gyroid	Pore size : 200 – 500 μm Porosity – 40%, 50%, 60%	Mechanical stability: TPMS > octet > cubic
Sun et al. (2022) [60]	SLM Ti64 TPMS gyroid, diamond and primitive	Sheet thickness : 200 – 400 μm	Elastic-brittle failure mechanism for all samples

3.2. Biological Performance of 3DP Ti64 scaffolds

The biological performance of the 3DP Ti64 scaffolds was explored using the static cell culture and biochemical assays. The cytocomptaibility, cell adherence and proliferation has been assessed by means of fluorescence microscopy and MTT assay.

3.2.1. Cytocompatibility Assessment

HOBs were exposed to cell medium with Ti64 and to cell medium without Ti64 (control) for a period of 14 days. On comparing the morphology and number of cells in the control with the cells exposed to Ti64, it was found that the HOBs in the Ti64 leachate exhibited similar nuclei morphology compared to the control as depicted in Figure 5. In addition, the cells proliferated in the leachate medium. This further reiterates the cytocompatibility of Ti64, which is FDA approved for biomedical applications. A number of research studies have substantiated the cytocomptaibility of Ti64 using osteoblasts. The study conducted by Huang et al. (2021) [28] studied the cytocompatibility of Ti64 by evaluating the scaffold degradation using indirect cytotoxicity and ion release test. It was noted that there was increase in cell proliferation on day 14 compared to day 7.

3.2.2. Impact of Pore Size on Cell Adherence and Cell Proliferation

Initial cell attachment on the scaffold surface is essential for scaffold – bone bonding. The scaffold surface must be conducive to facilitate the osseointegration. As depicted in Figure 5a–i, D300, C300 and G300 had more cells compared to their higher pore size counterparts.

 doi:10.20944/preprints202504.1850.v1

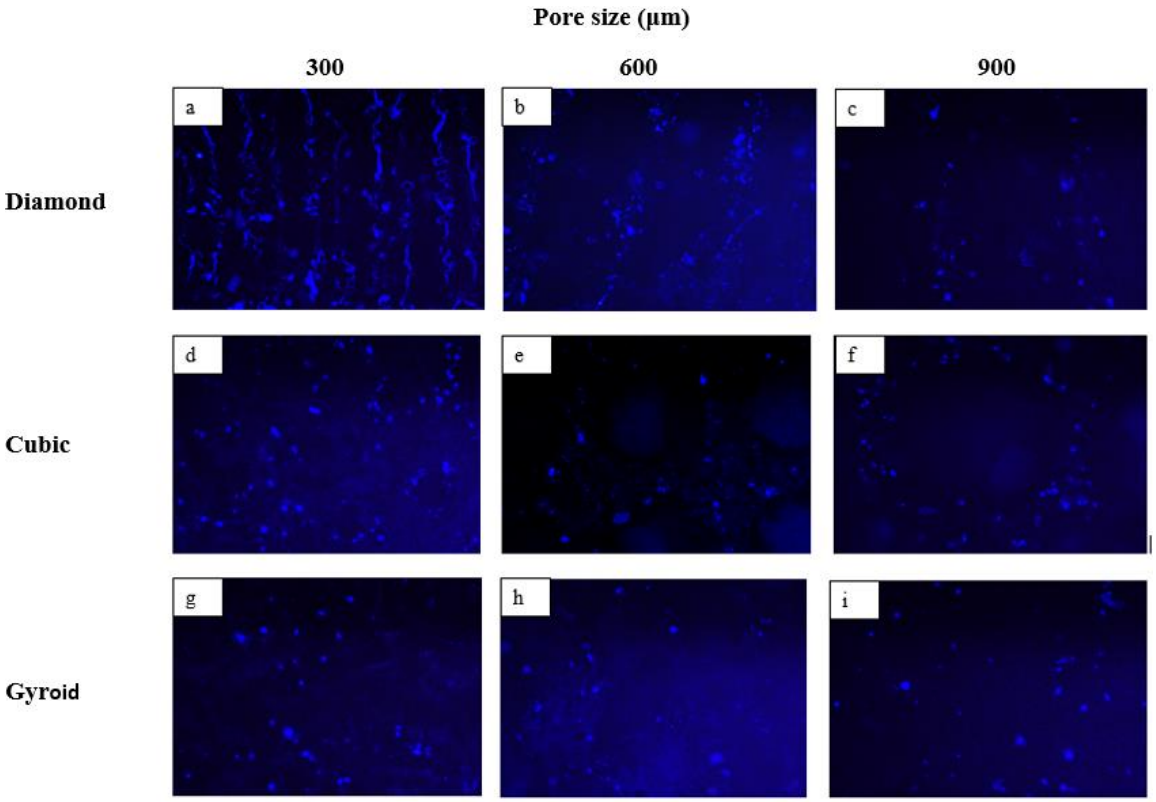

Figure 5. (**a**–**i**) Cell adherence using fluorescent imaging (magnification: 4×).

The number of cells on the surface decreased with an increase in pore size. It can be observed that initial cell adherence exhibited the following trend:

D300 > C300 > G300

Similar trend was followed by the 600 µm pore size group. However for the 900 µm pore size group, C900 had the maximum adherence followed by D900 and G900. It was observed that pore size was inversely proportional to cell adherence. The study by Nune et al. (2016) [65] studied the behaviour of osteoblasts on functionally graded 3DP Ti64 mesh structures. Similar to the results of the current study, Ti64 meshes had well-distributed and well-spread nuclei. Nune et al. (2016) [65] reported that non-porous Ti64 exhibited uniform distribution of cell nuclei whereas porous samples exhibited cell attachment on the struts and curved regions of the struts. This is similar to our findings. A smaller pore size provides larger surface area for cells to interact, thereby producing more interfacial force prior to falling through the pores. Hence, smaller pore sizes are expected to have more surface attachment of cells. This could be reason for more cells to be found on the surface of D300, C300 and G300.The diamond group had maximum cells adherence in the 300 and 600 group whereas the C900 reported superior adherence in the 900µm group. It has to be noted that cell adhesion is the first cellular event when an osteoblasts contact a scaffold surface. According to Xu et al. (2016) [66], cell adhesion impacts the proliferation, tissue formation and differentiation. As reported by Van Bael et al. (2012) [67], cell seeding efficiency indicative of cell adherence (on day 1) was significantly higher in the smallest pore size.

Though cell proliferation can be qualitatively assessed by means of fluorescent imaging using DAPI, quantitative assessment of cell proliferation mandates using MTT or similar assays. The MTT assay was performed in the current study to investigate the impact of varying the pore sizes and geometry. Figure 6 has depicted the results of the cell proliferation using the MTT assay.

 doi:10.20944/preprints202504.1850.v1

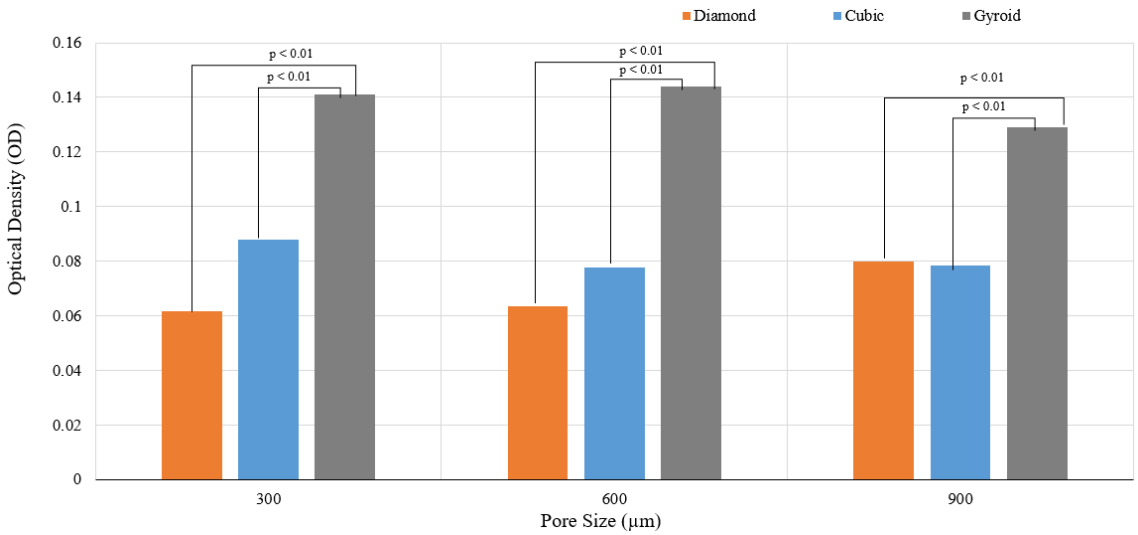

Figure 6. Results of Cell Proliferation at 7 days ($p < 0.01$).

It can be observed that both pore size and unit cell variation had an impact on the cell proliferation. The cell proliferation over 7 days was reported maximum for gyroid with the following trend:

G600 > G300 > G900

A statistically significant difference in the cell proliferation was reported between the diamond/gyroid and cubic/gyroid groups. Cell proliferation in both the strut-based lattices did not show any statistical significant difference, however, the sheet-based TPMS gyroid had substantially higher cell proliferation. The higher cell proliferation on G600 could be due to a balance between the pore size and surface adherence. It has to be noted that the actual pore size of the G600 and G900 samples are is 423 ± 12.5 µm and 710 ± 6.8 µm, respectively. The TPMS gyroid structures are characterized by high permeability in addition to slick and uniform surface. It is known for its absence of sharp corners, high surface area, and highly interconnected network and zero mean curvatures. It has to be noted that the mean surface curvature of the cancellous bone is close to zero; this promotes cell proliferation and tissue regeneration on such scaffolds. This could be one of the key reasons for the increased cell proliferation on the gyroid scaffolds. It has to be noted that the variation in the surface curvature may potentially lead to substantial changes in terms of the cell attachment rate, cell migration speed, and cell morphology including the cell spread area. Results similar to our study was reported by Wang et al. (2022) [56] who observed that cell viability of TPMS gyroid Ti64 was greater than the octet and cubic lattice structures. Wang et al. explored the relationship between ion release and type of lattice structure. Though we have not explored ion release, the aspect of cell viability is considered. It has to be noted that the scaffold surface area of the TPMS gyroid samples in the current study was higher than the cubic and diamond samples; this could also be one of the reasons for superior cell proliferation. The sharp struts and edges, acute corners of diamond and cubic structures may have limited the cell proliferation. Amongst the diamond and cubic samples, the following trend was observed for cell proliferation:

C300 > D900 > C900 > C600 > D600 > D300 (Figure 17)

The overall trend is as follows (Figure 17):

G600 > G300 > G900 > C300 > D900 > C900 > C600 > D600 > D300

As far as the diamond samples are concerned, D900 resulted in max cell proliferation. This contradicts the findings of Taniguchi et al. (2016) [27]. This could be because the cell proliferation was taken over 7 days; an extended period of MTT assessment with data points at 14, 21 and 28 days could substantiate the long-term cell proliferation. The study conducted by Taniguchi et al. (2016) [27] investigated the impact of pore size on bone ingrowth into porous Ti64 samples. Amongst the diamond lattice samples designed for pore sizes of 300, 600 and 900 µm with a constant porosity of

 doi:10.20944/preprints202504.1850.v1

65%, it was noted that the 600 μm sample (P600) exhibited maximum bone ingrowth at 2 weeks; this was followed by P900 and P300. The current study is based on results of in-vitro testing and may not substantiate in-vivo performance. The study conducted by Ran et al. (2018) [68] reported that cell seeding efficiency was highest for samples of 500 μm pore size (p500) followed by p700 and p900; there was statistically significant difference between the cell seeding efficiency amongst different pore sizes. As expected, the cell seeding efficiency decreased with increasing pore size. Ran et al. (2018) [68] also reported that cell proliferation increased with increasing in duration of seeding (7 days vs 14 days). At the end of 7 days, the cells on p700 exhibited higher viability whereas p900 exhibited had higher proliferation compared to p500 over 14 days of culture. Markhoff et al. (2015) [48] has recommended a pore size of 400 - 620 μm and a porosity of 76% for maximum metabolic activity. According to Markhoff et al. (2015) [48] Initial cell adhesion and cell bridging can be facilitated with lower pore sizes as they have higher surface area, thereby leading to increased cell proliferation. Mechanical stiffness may also have an impact on the metabolic activity as osteoblasts are mechano-sensitive [48]. However, lower pore sizes may limit the cell migration or lead to cell occlusion. As cells were reported to have been adhering to struts due to the surface area for initial adhesion, it is important to cater to apt strut and pore sizes.

The C300 samples facilitated initial cell adherence and proliferation and reported high cell numbers for the 7-day culture. The cells may not have had ample time for permeating into the pores and spreading on the internal regions of the scaffolds. It is imperative to conduct the cell proliferation over different time points to understand the impact of the pore size and the unit cell variation. However, the TPMS gyroid is superior to the strut-based lattices used in this study. In addition, the impact of pore size variation did not have statistical significance unlike the variation in unit cell.

Larger pore sizes can enhance vascularization and lead to enhanced osseointegration. However, smaller pores in the range of 400 – 600 μm facilitate early cell adherence due to focal adhesion [48]. The minimal pore size to stimulate bone ingrowth is 100 – 150 μm [69–72]. Pore sizes larger than 300 μm is capable of augmenting the capillary and new bone formation [70–72]. Pore sizes larger than 900 μm may limit the cell-bridging ability. Smaller pore sizes have more surface area for more tissue to form; this could be the reason the 300 μm pore sizes have initial cell adherence [71,72].The 150 μm - 900 μm pores permit the diffusion of waste and nutrients. As far as porosity is concerned, a porosity in the range of 40% - 70% is ideal for regulation of cell motility, nutrient and oxygen delivery [29]. In our study certain samples exhibited a porosity of > 50% which is in the range of the cancellous bone. This is ideal for cell proliferation and adherence. However, this could be the reason of compromised mechanical performance. An apposite balance between the biological and mechanical properties of a bone scaffold is necessary for facilitating osseointegration.

4. Conclusions

On analysis of the Ti64 samples, it was observed that an increase in the pore size increased the porosity considerably (as strut sizes were maintained constant). Owing to this, the E, σ_y and UCS reduced considerably with increased pore size. The study was able to understand the mode of failure with variation in pore sizes. As far as the suitability of the diamond unit cell for bone scaffolds are concerned, the D300 and 600 samples were suitable for cortical bone whereas D900 was slightly higher than E of trabecular bone. It has to be noted that D600 may not be suitable for high load bearing applications such as femur or tibia. Similar to the diamond samples, the cubic 300 and 600 samples (>50% porosity) had a modulus within the cortical bone range making it suitable for load-bearing applications. Since the porosity is high, the osteoblast adherence and growth could be enhanced. Although the C900 sample modulus is very slightly above the trabecular range, it can be used in regions where there the proportion of trabecular bone is higher than cortical bone. As far as the mode of failure is concerned, the C600 and C900 samples experienced failure by means of crushing potentially due to vertical strut failure. The C900 elastic modulus was higher than the trabecular bone (~ 2 times ED900). As far as G600 and G900 samples are concerned, E was well within the range of the cortical bone. The σ_y of G600 and G900 samples were much in the cortical bone range. It was

 doi:10.20944/preprints202504.1850.v1

concluded that the gyroid samples in the current study are not suitable for trabecular bone applications.

Leachate analysis on the 3DP Ti64 samples proved its cytocompatibility. The nuclei stained using DAPI and imaged using fluorescence microscopy indicated no difference in the nuclei morphology of osteoblasts cultured in cell medium with and without Ti64. The Ti64 D300, C300 and G300 had more cells compared to their higher pore size counterparts. The cell number on the Ti64 surface decreased with an increase in pore size. However for the cell proliferation, a different trend was noted. The TPMS gyroid had the highest cell numbers. Similar to the optimal pore size recommendations from research studies, a pore size range of 300 – 900 μm was found to be apt for apposite cell proliferation. However, more studies should be conducted to substantiate the impact of pore size and scaffold geometry on mechanical and biological performance of scaffolds.

Author Contributions: Conceptualization, P.N., S.M.C., and W.Y.Y.; Methodology, P.N., S.M.C., and W.Y.Y.; Software, P.N., S.M.C., and W.Y.Y.; Validation, P.N., S.M.C., and W.Y.Y.; Formal Analysis, P.N., S.M.C., and W.Y.Y.; Investigation, P.N., S.M.C., and W.Y.Y.; Resources, P.N., S.M.C., and W.Y.Y.; Data Curation, P.N., S.M.C., and W.Y.Y.; Writing—Original Draft Preparation, P.N., S.M.C., and W.Y.Y.; Writing—Review and Editing, P.N., S.M.C., and W.Y.Y.; Visualization, P.N., S.M.C., and W.Y.Y.; Supervision, P.N., S.M.C., and W.Y.Y.; Project Administration, P.N., S.M.C., and W.Y.Y.; Funding Acquisition, P.N., S.M.C., and W.Y.Y. All authors have read and agreed to the published version of the manuscript.

Funding: This study is partially funded by the National Additive Manufacturing Innovation Cluster (NAMIC) (Grant ID M22N2K0011), Agency for Science, Technology and Research (A*STAR), Singapore.

Data Availability Statement: Data available on request due to restrictions on privacy.

Acknowledgments: The authors would like to thank Nikon SLM Solutions Pte Ltd, Singapore for their research collaboration and support for sample fabrication.

Conflicts of Interest: The authors declare no conflicts of interest.

Abbreviations

The following abbreviations are used in this manuscript:

AM	Additive Manufacturing
BTE	Bone Tissue Engineering
3DP	3D printing
CSD	Critical-sized bone defects
ELI	Extra low interstitial
μCT	MicroCT
UCS	Ultimate compressive strength
HOB	Human osteoblast
PBS	Phosphate buffered saline
DAPI	4', 6-Diamidino-2-Phenylindole, Dihydrochloride
MTT	3-(4,5-dimethylthiazol-2-yl)-2,5-diphenyl-2H-tetrazolium bromide
OD	optical density
C	Cubic
TC	Truncated cube
TCO	Truncated cuboctahedron
RD	Rhombic dodecahedron
D	Diamond
RCO	rhombi cuboctahedron
S	Star
X	Cross
P	Primitive
I	I-WP
G	Gyroid

 doi:10.20944/preprints202504.1850.v1

References

1. Popov, V. V.; Muller-Kamskii, G.; Kovalevsky, A.; Dzhenzhera, G.; Strokin, E.; Kolomiets, A.; Ramon, J. Design and 3D-printing of titanium bone implants: brief review of approach and clinical cases. *Biomedical engineering letters*. **2018**, 8, 337- 344.
2. Ngo, T. D.; Kashani, A.; Imbalzano, G.; Nguyen, K. T.; Hui, D.. Additive manufacturing (3D printing): A review of materials, methods, applications and challenges. *Composites Part B: Engineering*. **2018**, 143, 172-196.
3. Ghorbani, F.; Li, D.; Ni, S.; Zhou, Y.; Yu, B. 3D printing of acellular scaffolds for bone defect regeneration: A review. *Materials Today Communications*. **2020**, 22. doi:10.1016/j.mtcomm.2020.100979.
4. Haleem, A.; Javaid, M.; Khan, R. H.; & Suman, R. 3D printing applications in bone tissue engineering. *Journal of Clinical Orthopedic Trauma.* **2020**, 11, S118-S124. doi:10.1016/j.jcot.2019.12.002.
5. Nauth, A.; Schemitsch, E.; Norris, B.; Nollin, Z.; Watson, J. T. Critical-Size Bone Defects: Is There a Consensus for Diagnosis and Treatment? *Journal of Orthopedic Trauma.* **2018**, 32, S7-S11. doi:10.1097/BOT.0000000000001115.
6. Koolen, M.; Amin Yavari, S.; Lietaert, K.; Wauthle, R.; Zadpoor, A. A.; Weinans, H. Bone Regeneration in Critical-Sized Bone Defects Treated with Additively Manufactured Porous Metallic Biomaterials: The Effects of Inelastic Mechanical Properties. *Materials (Basel)*. **2020**, 13. doi:10.3390/ma13081992.
7. Li, G.; Wang, L.; Pan, W.; Yang, F.; Jiang, W.; Wu, X.; Kong, X.; Dai, K.; Hao, Y. In vitro and in vivo study of additive manufactured porous Ti6Al4V scaffolds for repairing bone defects. *Scientific reports*. **2016**, 6, 1-11.
8. Putra, N. E.; Mirzaali, M. J.; Apachitei, I.; Zhou, J.; Zadpoor, A. A. Multi- material additive manufacturing technologies for Ti-, Mg-, and Fe-based biomaterials for bone substitution. *Acta Biomaterialia*. **2020**, 109, 1-20. doi:10.1016/j.actbio.2020.03.037.
9. Qiao, S.; Wu, D.; Li, Z.; Zhu, Y.; Zhan, F.; Lai, H.; Gu, Y. The combination of multi-functional ingredients-loaded hydrogels and three-dimensional printed porous titanium alloys for infective bone defect treatment. *Journal of Tissue Engineering*. **2020**, 11, 2041731420965797. doi:10.1177/2041731420965797.
10. Tumedei, M.; Savadori, P.; Del Fabbro, M. Synthetic Blocks for Bone Regeneration: A Systematic Review and Meta-Analysis. *International Journal of Molecular Sciences*. **2019**, 20, 4221. doi:10.3390/ijms20174221.
11. Noordin, N. N. F. N. M.; Ahmad, N.; Mariatti, M.; Yahaya, B. H.; Sulaiman, A. R.; Hamid, Z. A. A. A review on bioceramics scaffolds for bone defect in different types of animal models: HA and β-TCP. *Biomedical Physics & Engineering Express*. **2022**, 8**,** 052002.
12. Rupp, M.; Klute, L.; Baertl, S.; Walter, N.; Mannala, G. K.; Frank, L.; ... Kerschbaum, M. The clinical use of bone graft substitutes in orthopedic surgery in Germany—A 10-years survey from 2008 to 2018 of 1,090,167 surgical interventions. *Journal of Biomedical Materials Research Part B: Applied Biomaterials*. **2022**, 110, 350-357.
13. Ji, K.; Wang, Y.; Wei, Q.; Zhang, K.; Jiang, A.; Rao, Y.; Cai, X. Application of 3D printing technology in bone tissue engineering. *Bio-Design and Manufacturing*. **2018**, 1, 203-210.
14. Bose, S.; Vahabzadeh, S.; Bandyopadhyay, A. Bone tissue engineering using 3D printing. Materials Today. **2013**, 16, 496-504. doi:10.1016/j.mattod.2013.11.017.
15. Gao, C.; Wang, C.; Jin, H.; Wang, Z.; Li, Z.; Shi, C.; . . . Wang, J. Additive manufacturing technique-designed metallic porous implants for clinical application in orthopaedics. *RSC Advances*. **2018**, 8, 25210. doi:10.1039/c8ra04815k.
16. Giannitelli, S. M.; Accoto, D.; Trombetta, M.; Rainer, A. Current trends in the design of scaffolds for computer-aided tissue engineering. *Acta Biomater*. **2014**, 10, 580. doi:10.1016/j.actbio.2013.10.024.
17. Zhang, L.; Yang, G.; Johnson, B. N.; Jia, X. Three-dimensional (3D) printed scaffold and material selection for bone repair. *Acta biomaterialia*. **2019**, 84, 16.
18. Kanwar, S.; Vijayavenkataraman, S. Design of 3D printed scaffolds for bone tissue engineering: A review. *Bioprinting*. **2021**, 24, e00167.
19. El-Hajje, A.; Kolos, E. C.; Wang, J. K.; Maleksaeedi, S.; He, Z.; Wiria, F. E.; ... & Ruys, A. J. Physical and mechanical characterisation of 3D-printed porous titanium for biomedical applications. *Journal of Materials Science: Materials in Medicine.* **2014**, 25, 2471-2480.

 doi:10.20944/preprints202504.1850.v1

20. Ahsan, M. M.; Student, M. S. 3D printing and titanium alloys: a paper review. *Eur. Acad. Res*. **2016**, 3, 11144-11154.
21. Dziaduszewska, M.; Zieliński, A. Structural and material determinants influencing the behavior of porous Ti and its alloys made by additive manufacturing techniques for biomedical applications. *Materials*. **2021**, 14, 712.
22. Wubneh, A.; Tsekoura, E. K.; Ayranci, C.; Uludağ, H. Current state of fabrication technologies and materials for bone tissue engineering. *Acta Biomaterialia.* **2018**, 80, 1-30.
23. Jariwala, S. H.; Lewis, G. S.; Bushman, Z. J.; Adair, J. H.; Donahue, H. J. 3D printing of personalized artificial bone scaffolds. *3D printing and additive manufacturing.* **2015**, 2, 56-64.
24. Brunello, G.; Sivolella, S.; Meneghello, R.; Ferroni, L.; Gardin, C.; Piattelli, A.; ... & Bressan, E. Powder-based 3D printing for bone tissue engineering. *Biotechnology advances*. **2016**, 34, 740.
25. Germaini, M. M.; Belhabib, S.; Guessasma, S.; Deterre, R.; Corre, P.; Weiss, P. Additive manufacturing of biomaterials for bone tissue engineering–A critical review of the state of the art and new concepts. *Progress in Materials Science*. **2022**, 100963.
26. Zhang, Y.; Sun, N.; Zhu, M.; Qiu, Q.; Zhao, P.; Zheng, C.; Lu, T. The contribution of pore size and porosity of 3D printed porous titanium scaffolds to osteogenesis. *Biomaterials Advances*, **2022**, 133, 112651.
27. Taniguchi, N.; Fujibayashi, S.; Takemoto, M.; Sasaki, K.; Otsuki, B.; Nakamura, T.; Matsushita, T.; Kokubo, T.; Matsuda, S. Effect of pore size on bone ingrowth into porous titanium implants fabricated by additive manufacturing: An in vivo experiment. *Materials Science and Engineering: C*, **2016**, 59, 690-701.
28. Huang, G.; Pan, S. T.; Qiu, J. X.. The osteogenic effects of porous tantalum and titanium alloy scaffolds with different unit cell structure. C*olloids and Surfaces B: Biointerfaces.* **2022**, 210, 112229.
29. Pei, X.; Zhang, B.; Fan, Y.; Zhu, X.; Sun, Y.; Wang, Q.; ... Zhou, C. Bionic mechanical design of titanium bone tissue implants and 3D printing manufacture. *Materials Letters.* **2017**, 208, 133-137.
30. Zhang, B.; Pei, X.; Zhou, C.; Fan, Y.; Jiang, Q.; Ronca, A.; D'Amora, U.; Chen, Y.; Li, H.; Sun, Y.; Zhang, X. The biomimetic design and 3D printing of customized mechanical properties porous Ti6Al4V scaffold for load-bearing bone reconstruction. *Materials & Design.* **2018**, 152, 30-39.
31. Yavari, S. A.; Ahmadi, S. M.; Wauthle, R.; Pouran, B.; Schrooten, J.; Weinans, H.; Zadpoor, A. A. Relationship between unit cell type and porosity and the fatigue behavior of selective laser melted meta-biomaterials. *J. of the mechanical behavior of biomedical materials*. **2015**, 43, 91-100.
32. Liu, F.; Zhang, D. Z.; Zhang, P.; Zhao, M.; Jafar, S. Mechanical properties of optimized diamond lattice structure for bone scaffolds fabricated via selective laser melting. *Materials*. **2018**, 11, 374.
33. Wally, Z. J.; Haque, A. M.; Feteira, A.; Claeyssens, F.; Goodall, R.; Reilly, G. C. Selective laser melting processed Ti6Al4V lattices with graded porosities for dental applications. *Journal of the Mechanical Behavior of Biomedical Materials.* **2019**, 90, 20-29.
34. Deng, F.; Liu, L.; Li, Z.; Liu, J.. 3D printed Ti6Al4V bone scaffolds with different pore structure effects on bone ingrowth. *Journal of Biological Engineering*. **2021**, 15, 1-13.
35. Choy, S. Y.; Sun, C. N.; Leong, K. F.; Wei, J. Compressive properties of Ti-6Al-4V lattice structures fabricated by selective laser melting: Design, orientation and density. *Additive Manufacturing*. **2017**, 16, 213-224.
36. Martinez-Marquez, D.; Delmar, Y.; Sun, S.; Stewart, R. A. Exploring Macroporosity of Additively Manufactured Titanium Metamaterials for Bone Regeneration with Quality by Design: A Systematic Literature Review. *Materials*. **2020**, 13, 4794. [Online]. Available: https://www.mdpi.com/1996-1944/13/21/4794.
37. Zaharin, H.A.; A. Rani, M.A.; Ginta, T.L.; Azam, F. I. Additive Manufacturing Technology for Biomedical Components: A review. *IOP Conference Series: Materials Science and Engineering*. **2018**, 328, 012003. doi: 10.1088/1757-899X/328/1/012003
38. Sun, J.; Yang, Y.; Wang, D. Mechanical properties of a Ti6Al4V porous structure produced by selective laser melting. *Materials & Design.* **2013**, 49, 545-552. doi: https://doi.org/10.1016/j.matdes.2013.01.038.
39. Yuan, L.; Ding, S.; Wen, C. Additive manufacturing technology for porous metal implant applications and triple minimal surface structures: A review. *Bioactive Materials.* **2019**, 4, 56-70. doi: https://doi.org/10.1016/j.bioactmat.2018.12.003.

 doi:10.20944/preprints202504.1850.v1

40. Ni, J.; Ling, H.; Zhang, S.; Wang, Z.; Peng, Z.; Benyshek, C.; Zan, R.; Miri, A.K.; Li, Z.; Zhang, X.; Lee, J.A. Three-dimensional printing of metals for biomedical applications. *Materials Today Bio.* **2019**, 3, 100024.
41. Geetha, M.; Singh, A.K.; Asokamani, R.; Gogia, A.K. Ti based biomaterials, the ultimate choice for orthopaedic implants – A review. *Progress in Materials Science.* **2009**, 54, 397-425. doi: https://doi.org/10.1016/j.pmatsci.2008.06.004.
42. Liu, G.; Zhang, X.; Chen, X.; He, Y.; Cheng, L.; Huo, M.; ... & Lu, J. Additive manufacturing of structural materials. *Materials Science and Engineering: R: Reports.* **2021**, 145, 100596.
43. Shah, F. A.; Trobos, M.; Thomsen, P.; Palmquist, A. Commercially pure titanium (cp-Ti) versus titanium alloy (Ti6Al4V) materials as bone anchored implants—Is one truly better than the other?. *Materials Science and Engineering: C.* **2016**, 62, 960-966.
44. Roseti, L.; Parisi, V.; Petretta, M.; Cavallo, C.; Desando, G.; Bartolotti, I.; & Grigolo, B. Scaffolds for bone tissue engineering: state of the art and new perspectives. *Materials Science and Engineering: C.* **2017**, 78, 1246-1262.
45. Jiao, L.; Chua, Z.; Moon, S.; Song, J.; Bi, G. ; Zheng, H. Y. Femtosecond Laser Produced Hydrophobic Hierarchical Structures on Additive Manufacturing Parts, *Nanomaterials*. **2018**, 8, 601. doi: 10.3390/nano8080601.
46. Chen, S. Y.; Huang, J. C.; Pan, C. T.; Lin, C. H.; Yang, T. L.; Huang, Y. S.; Yang, C. C. Microstructure and mechanical properties of open-cell porous Ti-6Al-4V fabricated by selective laser melting. *Journal of Alloys and Compounds.* **2017**, 713, 248-254.
47. Alomar, Z.; Concli, F. A review of the selective laser melting lattice structures and their numerical models. *Advanced Engineering Materials.* **2020**, 22, 2000611.
48. Markhoff, J.; Krogull, M.; Schulze, C.; Rotsch, C.; Hunger, S.; Bader, R. Biocompatibility and inflammatory potential of titanium alloys cultivated with human osteoblasts, fibroblasts and macrophages. *Materials.* **2015**, 10, 52.
49. Rotaru, H.; Schumacher, R.; Kim, S. G.; Dinu, C. Selective laser melted titanium implants: a new technique for the reconstruction of extensive zygomatic complex defects. *Maxillofacial Plastic and Reconstructive Surgery*. **2015**, 37, 1-6.
50. Wu, M. W.; Chen, J. K.; Lin, B. H.; Chiang, P. H.; Tsai, M. K. Compressive fatigue properties of additive-manufactured Ti-6Al-4V cellular material with different porosities. *Materials Science and Engineer*ing*: A.* **2020**, 790, 139695.
51. Fousová, M.; Vojtěch, D.; Kubásek, J.; Jablonská, E.; Fojt, J. Promising characteristics of gradient porosity Ti-6Al-4V alloy prepared by SLM process. *Journal of the Mechanical Behavior of Biomedical Materials*. **2017**, 69, 368-376.
52. Zaharin, H. A.; Abdul Rani, A. M.; Azam, F. I.; Ginta, T. L.; Sallih, N.; Ahmad, A.; ... Zulkifli, T. Z. A. Effect of unit cell type and pore size on porosity and mechanical behavior of additively manufactured Ti6Al4V scaffolds. *Materials*. **2018**, 11, 2402.
53. Yavari, S. A.; Wauthlé, R.; van der Stok, J.; Riemslag, A. C.; Janssen, M.; Mulier, M.; ... Zadpoor, A. A. Fatigue behavior of porous biomaterials manufactured using selective laser melting. *Materials Science and Engineering: C*. **2013**, 33, 4849-4858.
54. Benedetti, M.; Santus, C. Notch fatigue and crack growth resistance of Ti-6Al-4V ELI additively manufactured via selective laser melting: A critical distance approach to defect sensitivity. *International Journal of Fatigue*. **2019**, 121, 281-292.
55. Ahmadi, S. M.; Amin Yavari, S.; Wauthle, R.; Pouran, B.; Schrooten, J.; Weinans, H.; Zadpoor, A. A. Additively manufactured open-cell porous biomaterials made from six different space-filling unit cells: The mechanical and morphological properties. *Materials*. **2015**, 8, 1871-1896.
56. Wang, N.; Meenashisundaram, G. K.; Kandilya, D.; Fuh, J. Y. H.; Dheen, S. T.; & Kumar, A. S. A biomechanical evaluation on Cubic, Octet, and TPMS gyroid Ti6Al4V lattice structures fabricated by selective laser melting and the effects of their debris on human osteoblast-like cells. *Biomaterials Advances*. **2022**, 137, 212829.

 doi:10.20944/preprints202504.1850.v1

57. Bobbert, F. S. L.; Lietaert, K.; Eftekhari, A. A.; Pouran, B.; Ahmadi, S. M.; Weinans, H.; Zadpoor, A. A. Additively manufactured metallic porous biomaterials based on minimal surfaces: A unique combination of topological, mechanical, and mass transport properties. *Acta biomaterialia*. **2017**, 53, 572-584.
58. Weißmann, V.; Bader, R.; Hansmann, H.; Laufer, N. Influence of the structural orientation on the mechanical properties of selective laser melted Ti6Al4V open-porous scaffolds. *Materials & Design*. **2016**, 95, 188-197.
59. Van Hooreweder, B.; Apers, Y.; Lietaert, K.; & Kruth, J. P. Improving the fatigue performance of porous metallic biomaterials produced by Selective Laser Melting. *Acta biomaterialia*. **2017**, 47, 193-202.
60. Sun, Q.; Sun, J.; Guo, K.; Wang, L. Compressive mechanical properties and energy absorption characteristics of SLM fabricated Ti6Al4V triply periodic minimal surface cellular structures. *Mechanics of Materials*. **2022**, 166, 104241.
61. Yánez, A.; Cuadrado, A.; Martel, O.; Afonso, H.; Monopoli, D. Gyroid porous titanium structures: A versatile solution to be used as scaffolds in bone defect reconstruction. *Materials & Design*. **2018**, 140, 21-29.
62. Naghavi, S. A.; Tamaddon, M.; Marghoub, A.; Wang, K.; Babamiri, B. B.; Hazeli, K.; ... Liu, C. Mechanical Characterisation and Numerical Modelling of TPMS-Based Gyroid and Diamond Ti6Al4V Scaffolds for Bone Implants: An Integrated Approach for Translational Consideration. *Bioengineering*. **2022**, 9, 504.
63. Barber, H.; Kelly, C. N.; Nelson, K.; Gall, K. Compressive anisotropy of sheet and strut based porous Ti–6Al–4V scaffolds. *Journal of the Mechanical Behaviour of Biomedical Materials*. **2021**, 115, 104243.
64. Li, L.; Shi, J.; Zhang, K.; Yang, L.; Yu, F.; Zhu, L.; ... Jiang, Q. Early osteointegration evaluation of porous Ti6Al4V scaffolds designed based on triply periodic minimal surface models. *Journal of Orthopaedic Translation*. **2019**, 19, 94-105.
65. Nune, K. C.; Kumar, A.; Misra, R. D. K.; Li, S. J.; Hao, Y. L.; Yang, R. Osteoblast functions in functionally graded Ti-6Al-4 V mesh structures. *Journal of Biomaterials Applications*. **2016**, 30, 1182-1204.
66. Xu, Y.; Zhang, D.; Zhou, Y.; Wang, W.; & Cao, X. Study on topology optimization design, manufacturability, and performance evaluation of Ti-6Al-4V porous structures fabricated by selective laser melting (SLM). *Materials*. **2017**, 10, 1048.
67. Van Bael, S.; Chai, Y. C.; Truscello, S.; Moesen, M.; Kerckhofs, G.; Van Oosterwyck, H.; ... & Schrooten, J. J. A. B. The effect of pore geometry on the in vitro biological behavior of human periosteum-derived cells seeded on selective laser-melted Ti6Al4V bone scaffolds. *Acta biomaterialia*. **2012**, 8, 2824.
68. Ran, Q.; Yang, W.; Hu, Y.; Shen, X.; Yu, Y.; Xiang, Y.; Cai, K. Osteogenesis of 3D printed porous Ti6Al4V implants with different pore sizes. *Journal of the Mechanical Behavior of Biomedical Materials*. **2018**, 84, 1-11.
69. Rodríguez-Montaño, Ó. L.; Cortés-Rodríguez, C. J.; Uva, A. E.; Fiorentino, M.; Gattullo, M.; Monno, G.; Boccaccio, A. Comparison of the mechanobiological performance of bone tissue scaffolds based on different unit cell geometries. *Journal of the mechanical behavior of biomedical materials*. **2018**, 83, 28-45.
70. Yang, L.; Gao, Q.; Ge, L.; Zhou, Q.; Warszawik, E. M.; Bron, R.; ... van Rijn, P. Topography induced stiffness alteration of stem cells influences osteogenic differentiation. *Biomaterials science*. **2020**, 8, 2638-2652.
71. Yan, C.; Hao, L.; Hussein, A.; Young, P. Ti–6Al–4V triply periodic minimal surface structures for bone implants fabricated via selective laser melting. *Journal of the Mechanical Behavior of Biomedical Materials.* **2015**, 51, 61-73.
72. Fukuda, A.; Takemoto, M.; Saito, T.; Fujibayashi, S.; Neo, M.; Pattanayak, D. K.; ... Nakamura, T. Osteoinduction of porous Ti implants with a channel structure fabricated by selective laser melting. *Acta Biomaterialia.* **2011**, 7, 2327-2336.